

## Vortex shedding in confined swirling flow of polymer solutions

Shinji Tamano,<sup>a)</sup> Motoyuki Itoh, Yuichiro Ide, and Kazuhiko Yokota  
 Graduate School of Engineering, Nagoya Institute of Technology, Gokiso-cho, Showa-ku, Nagoya,  
 Aichi 466-8555, Japan

(Received 14 June 2006; accepted 18 January 2007; published online 28 February 2007)

The unsteady swirling flow of an aqueous polymer solution due to a rotating disk in a cylindrical casing was investigated using the flow visualization technique. As the aqueous polymer solution, polyacrylamide solutions whose concentrations were 0.025, 0.1, 0.2, 0.5, 0.8, and 1.0 wt% were used. The unsteady secondary flow patterns were classified using the Reynolds and elastic numbers. We found a new phenomenon of vortex shedding in which the ring vortex formed near the rotating disk was periodically shed away from the rotating disk in the unsteady flow regime. The nonaxisymmetric ring vortex was also observed for the higher Reynolds number compared to that of the axisymmetric ring vortex. The dependence of the period of vortex shedding on the Reynolds number was clarified. © 2007 American Institute of Physics. [DOI: 10.1063/1.2709705]

### I. INTRODUCTION

The study of confined swirling flows of viscoelastic fluids is attractive from a scientific point of view for constructing rheological models owing to the well-defined boundary condition, and its understanding is of great importance in many process engineering applications. Therefore, many experimental studies have been conducted to examine the fundamental flow behavior in the confined swirling flow of viscoelastic fluids. A pioneering study on the viscoelastic swirling flow due to a rotating disk in a cylindrical casing was conducted by Hill,<sup>1</sup> who observed that the secondary flow direction of viscoelastic fluids was opposite to that of Newtonian fluids due to the elastic force. Recently, Day *et al.*<sup>2</sup> observed the ring vortex near the center of the rotating disk, and Escudier and Cullen<sup>3</sup> found the double cell structure of the secondary flow using flow visualization technique. More recently, Moroi *et al.*<sup>4</sup> and Itoh *et al.*<sup>5</sup> have investigated velocity fields of the confined swirling flow using particle tracking velocimetry (PTV) and laser Doppler velocimetry (LDV) measurements, respectively. Moreover, Stokes *et al.*<sup>6,7</sup> have published comprehensive studies on inertia and elasticity effects using particle image velocimetry (PIV) measurements. These experimental studies have revealed the steady secondary flow at relatively low Reynolds number, and have yielded a lot of information valuable for numerical calculations<sup>8–12</sup> of viscoelastic fluids with various constitutive equation models.

In addition to the study on enclosed steady swirling flows of viscoelastic fluids, elastic instability<sup>13–17</sup> and elastic turbulence<sup>18,19</sup> for swirling flows between stationary and rotating disks in viscoelastic fluids have also been carried out. However, there have been fewer studies on unsteady secondary flows at relatively high Reynolds number, comparing to studies on steady swirling flows. Stokes and Boger<sup>20</sup> investigated the unsteady (chaotic) secondary flow using flow visualization, and presented the stability boundary diagram for

the confined swirling flow of polyacrylamide (PAA) fluids. But, the unsteady confined swirling flow of viscoelastic fluids remains unclear.

In this study, using the sectional and three-dimensional flow visualization, we investigate the unsteady flow patterns in the confined swirling flow of polymer solutions at relatively high Reynolds number. In particular, we focus on an attractive phenomenon of the vortex shedding observed, which has not been reported as far as we know.

### II. EXPERIMENTAL APPARATUS AND PROCEDURE

The experimental apparatus used in the present study is shown in Fig. 1. The main body consists of a rotating disk enclosed in a casing. The surface of the rotating disk is smooth, and the outside diameter is 180 mm ( $R=90$  mm). The disk is painted black to reduce the effect of reflected light. The aspect ratio of the distance  $H$  between the casing end wall and the rotating disk to the radius of the rotating disk  $R$  was fixed to  $H/R=2.0$ . The disk is driven by a motor and decelerator with an inverter control. The clear acrylic casing is cylindrical with an inner diameter of 181 mm. The exterior is rectangular, with a length on one side of 215 mm, to minimize the effect of light refraction while observing cross sections. In this study,  $r$ ,  $\theta$ , and  $z$  represent the radial, azimuthal, and axial directions, respectively, and their origin is at the center of the upper stationary disk (Fig. 1).

The working fluids were polymer solutions of polyacrylamide (Sanfloc AH70P, molecular weight of two to four million, Sanyo Kasei Kogyo, Ltd.), which was dissolved in tap water and was mixed by hand to prevent degradation. The concentrations of polyacrylamide solutions were 0.025, 0.1, 0.2, 0.5, 0.8, and 1.0 wt%. The shear viscosity  $\eta$  of the working fluid was measured using a cone-and-plate-type viscometer (Tokimec, Visco-Eld, cone angle  $\theta=3.00^\circ$ , diameter  $d=28.0$  mm, and  $\theta=1.34^\circ$ ,  $d=48.0$  mm) and a cone-and-plate-type rheometer (Rheology, MR-500,  $\theta=2.04^\circ$ ,  $d=40.0$  mm). The first normal stress difference  $N_1$  was measured using the cone-and-plate-type rheometer (MR-500).

<sup>a)</sup>Electronic mail: tamano.shinji@nitech.ac.jp

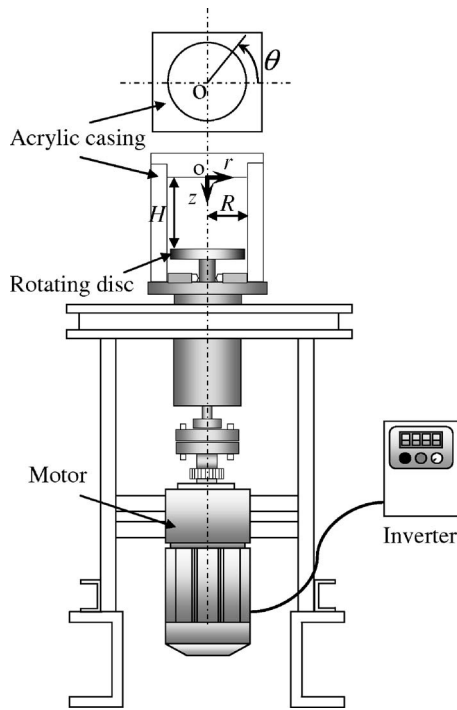
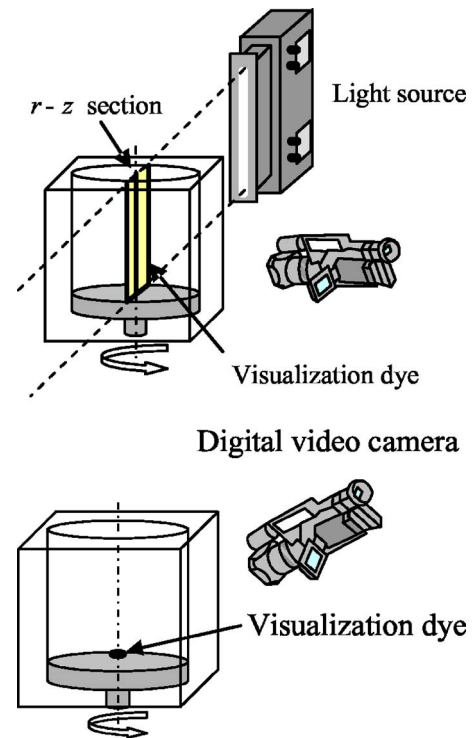


FIG. 1. Experimental apparatus.

FIG. 2. Flow visualization method: (a)  $r$ - $z$  section, (b) three-dimensional.

The uncertainty intervals of the data for  $\eta$  and  $N_1$  are 5% and 7%, respectively, of their absolute values. Measurements of  $\eta$  and  $N_1$  were conducted at the solution temperature  $T = 20^\circ\text{C}$ .

As a visualization dye, the mixture of Rhodamine B and the working fluid (PAA solution) was used. For the sectional visualization, the visualization dye was quasisteadily injected at the black line in Fig. 2(a) using a homemade injector, and the meridian section ( $r$ - $z$  section) was illuminated by the slit light source (Halogen, output: 1500 W, slit width: 3 mm). After increasing the rotation speed of the disk quasisteadily, the streak line was observed. For the three-dimensional visualization near the rotating disk, the visualization dye was quasisteadily injected only at the center of the rotating disk [the black point in Fig. 2(b)], after increasing the rotation speed quasisteadily, and maintaining it for half an hour. The images obtained for sectional and three-dimensional flow visualizations were captured by a digital video camera (DCR-VX2000, Sony, Ltd.).

### III. RESULTS

#### A. Rheological properties

Figures 3(a) and 3(b) show measurements of the shear viscosity  $\eta$  and the first normal stress difference  $N_1$  at the solution temperature  $T = 20^\circ\text{C}$ , respectively. In these figures, reference data available<sup>21–23</sup> were also presented. The solid lines represent the fitting curves of the Giesekus model.<sup>24</sup> The shear viscosity  $\eta$  increases with the increase of the concentration  $C$  of PAA fluid. Shear-thinning can also be observed where the shear viscosity decreases gradually with the increase in shear rate  $\dot{\gamma}$ . The first normal stress difference  $N_1$  increases with increasing both  $C$  and  $\dot{\gamma}$ . It was confirmed that

the shear viscosity and the first normal stress difference hardly changed before and after a test run, which indicates no appreciable degradation of working fluids during a test run. The density  $\rho$  of water was used for polymer solutions.

Table I shows Giesekus model parameters  $\eta_0$ ,  $\alpha$ ,  $\lambda$ , and  $\beta$ , which were obtained by fitting the Giesekus model curve with measurements of  $\eta$  and  $N_1$  best.  $\eta_0$  and  $\lambda$  are the zero shear viscosity and relaxation time, respectively.  $\alpha$  is the mobility factor, which is between 0 and 1.<sup>24</sup>  $\beta = \eta_s / \eta_0$  represents the ratio of the shear viscosity  $\eta_s$  of water to the zero shear viscosity  $\eta_0$  of solutions. Note that the Giesekus model curve coincides with the measurement of  $\eta$  better, rather than the measurement of  $N_1$ . The relaxation time  $\lambda$  for PAA 0.025 and 0.8 wt% was obtained by using the relation between the concentration of solution  $C$  wt% and the relaxation time  $\lambda$  s,  $\lambda = 13.4C^{0.654}$  which was derived by the interpolation given by the other data.

In the present study, the Reynolds number  $\text{Re}_0$  and elastic number  $E_0$  are defined as follows:

$$\text{Re}_0 = \frac{\rho R^2 \Omega}{\eta_0}, \quad (1)$$

$$E_0 = \frac{\lambda \eta_0}{\rho R^2}. \quad (2)$$

Here,  $\Omega$  is the angular velocity of the rotating disk and was varied from 1 to 37 rad/s in the present study.  $\text{Re}_0$  and  $E_0$  are evaluated by Giesekus model parameters shown in Table I. The elastic number  $E_0$  increases with the increase of the concentration  $C$ , and it is constant for a value of  $C$ . The apparent Reynolds number  $\text{Re}$  and elastic number  $E$  are also defined as follows:

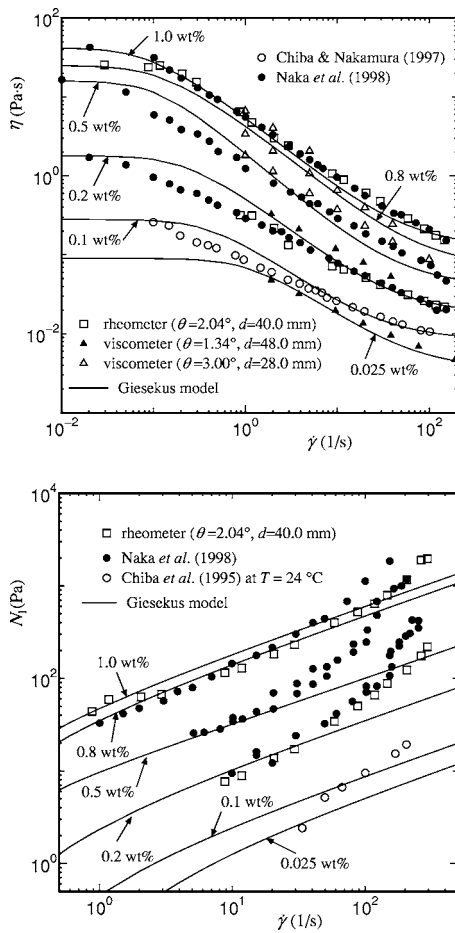


FIG. 3. Rheological properties for PAA solutions at  $T=20^\circ\text{C}$ : (a) Shear viscosity, (b) first normal stress difference.

$$\text{Re} = \frac{\rho R^2 \Omega}{\eta}, \quad (3)$$

$$E = \frac{\lambda_m \eta}{\rho R^2}, \quad (4)$$

where  $\lambda_m = N_1 / (2\eta\dot{\gamma}^2)$  is the Maxwell relaxation time and is dependent on the shear rate. Note that  $\lambda_m$  and  $\eta$  are given by assuming that  $\dot{\gamma} = \Omega$ .

TABLE I. Giesekus model parameters for PAA solutions.

$C$ (wt%)	$\eta_0$ (Pa s)	$\alpha$	$\lambda$ (s)	$\beta$	$E_0$
0.025	$9.0 \times 10^{-2}$	$1.2 \times 10^{-1}$	1.2	$4.0 \times 10^{-2}$	$1.3 \times 10^{-2}$
0.1	$2.8 \times 10^{-1}$	$1.5 \times 10^{-1}$	3.0	$3.0 \times 10^{-2}$	$1.0 \times 10^{-1}$
0.2	1.8	$2.0 \times 10^{-1}$	5.0	$1.0 \times 10^{-2}$	1.1
0.5	16	$6.0 \times 10^{-1}$	7.0	$2.5 \times 10^{-2}$	14
0.8	25	$1.2 \times 10^{-1}$	12	$2.8 \times 10^{-3}$	37
1.0	42	$1.5 \times 10^{-1}$	15	$3.0 \times 10^{-3}$	78

## B. Secondary flow patterns

In the unsteady flow regime presented by Stokes and Boger,<sup>20</sup> the unsteady flow behavior observed in the meridian section were classified into six kinds of flow patterns as follows.

(1) Type RT (reverse transition): The secondary flow, whose direction is opposite to that of Newtonian fluid, i.e., inward near the rotating disk in the radial direction, is formed. This reverse flow pattern is generated due to the elastic stress,<sup>1,5,7,20</sup> and it is termed “type R” in the present study. The secondary flow pattern, in which an unsteady spiral vortex appears in the vicinity of the central axis in addition to type R, is termed “type RT,” which has also been reported in the previous studies.<sup>2,4,5,7,20</sup> The typical flow pattern for type RT is illustrated in Fig. 4(a).

(2) Type DCT (double cell transition): The flow pattern, in which a double-cell structure where the two cells are aligned laterally in the radial direction is formed, is termed “type DC,” which has been reported in the previous study.<sup>3,5,7</sup> Figure 4(b) shows the flow pattern including an unsteady spiral vortex in the vicinity of the central axis in addition to type DC, which is termed “type DCT.” The flow pattern similar to type DCT has also been reported by Stokes *et al.*<sup>7</sup>

(3) Type NT (Newtonian transition): The flow pattern, in which the flow direction of the secondary flow is the same as that of Newtonian fluids, is termed “type N.” The flow pattern, in which the flow near the rotating axis is unsteady in addition to type N, is termed “type NT.” Typical secondary flow pattern for type NT is shown in Fig. 4(c). The flow pattern similar to type NT has been also mentioned in the study of Stokes *et al.*<sup>7</sup>

(4) Type VB (vortex breakdown): The flow pattern, in which the flow around the rotating axis is unstable, and the axial flow along the rotating axis cannot be observed, is termed “type VB,” since the flow pattern is somewhat similar to the vortex breakdown observed by Stokes *et al.*,<sup>6</sup> as shown in Fig. 4(d).

(5) Type NU (nonperiodic unsteady): We call the unsteady and unstable flow “type NU.” We cannot present the typical flow pattern for type NU, since the flow behavior seems to be chaotic.

(6) Type VS (vortex shedding): The ring rotax is formed near the rotating disk, and then it is periodically shed away from near the rotating disk. This flow pattern is termed “type VS.” The vortex shedding phenomenon observed in confined swirling flows of viscoelastic fluids has not been reported as far as we know. Therefore, we examine the phenomenon of the vortex shedding (type VS) in detail in the following sections.

Using the Reynolds number  $\text{Re}_0$  and the elastic number  $E_0$ , the secondary flow patterns observed in the present study are classified as shown in Fig. 5. Readers are referred to our previous studies,<sup>4,5</sup> in which the secondary flow patterns in the steady flow regime have been thoroughly examined. For PAA 0.025 wt% in which the elastic number is smallest, the flow pattern changes with increasing  $\text{Re}_0$  to type DCT, type

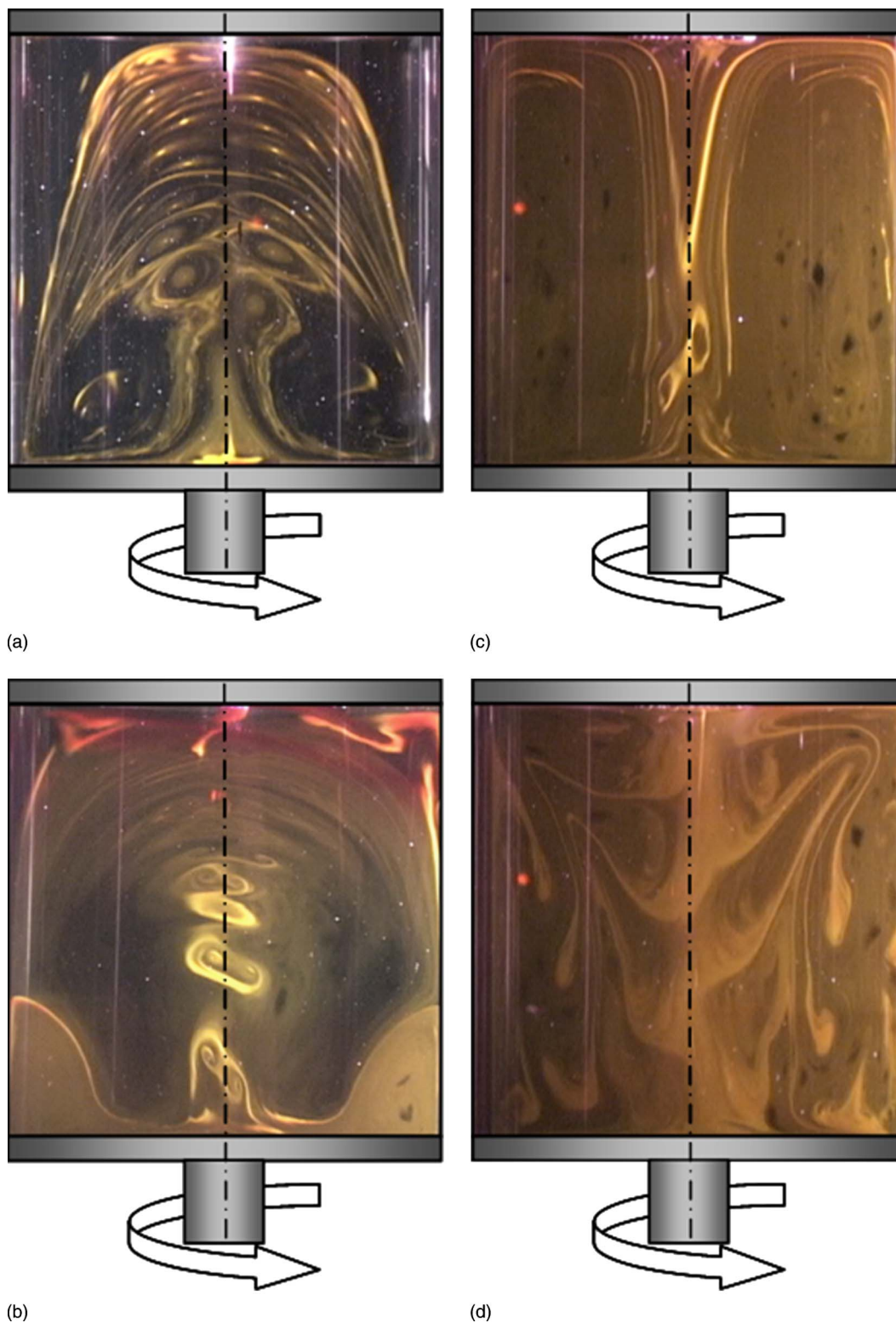


FIG. 4. Sectional flow visualization of typical flow patterns: (a) Type RT for PAA 0.2 wt% at  $Re_0=6.7$ , (b) type DCT for PAA 0.025 wt% at  $Re_0=2.7 \times 10^2$ , (c) type NT for PAA 0.025 wt% at  $Re_0=7.1 \times 10^2$ , and (d) type VB for PAA 0.025 wt% at  $Re_0=1.6 \times 10^3$ .

NT, and type VB. As the Reynolds number increases, the structure of the secondary flow changes to type RT, type VS, type NU, and type NT for PAA 0.1 and 0.2 wt%, and to type RT, type VS, and type NU for PAA 0.5, 0.8, and 1.0 wt%, respectively. The vortex shedding (type VS) was observed for PAA 0.1, 0.2, 0.5, 0.8, and 1.0 wt%. The lower critical

Reynolds number for type VS increases with the decrease in the concentration of PAA solutions, i.e., the elastic number. Note that the regime of vortex breakdown (type VB), which is fascinating, has not been identified enough owing to the limitation of the performance of the motor and decelerator used.

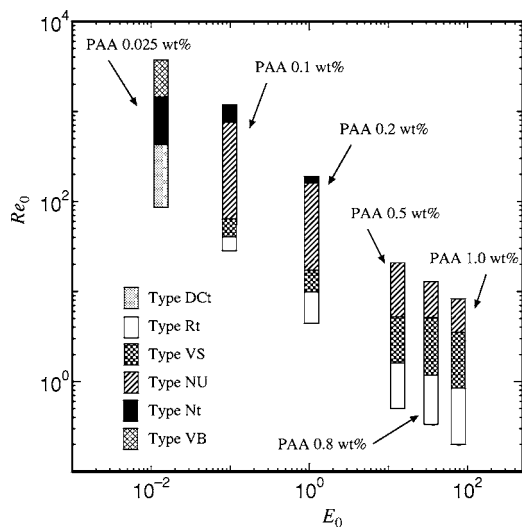
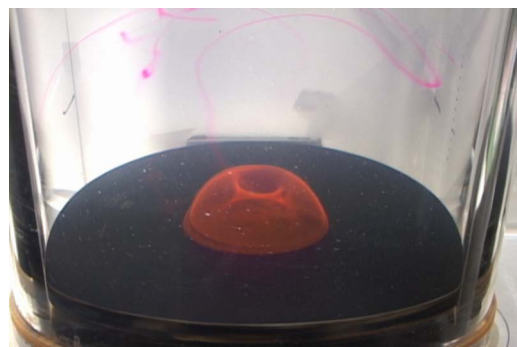


FIG. 5. Unsteady flow patterns for PAA solutions.

### C. Vortex shedding

The photograph of three-dimensional flow visualization for PAA 0.5 wt% at  $Re_0=2.1$  is shown in Fig. 6. It was found that the ring vortex, which is about one-third the size of the diameter of the rotating disk, was formed in the vicinity of the central axis near the rotating disk [Fig. 6(a)], and sometime later the ring vortex was shed away from the rotating disk in the axial direction while retaining its shape [Fig.



(a)



(b)

FIG. 6. Three-dimensional visualization of ring vortex for PAA 0.5 wt% at  $Re_0=2.1$ : (a) Ring vortex, (b) vortex shedding.

6(b)]. Note that the vortex shedding is not related to the perturbation due to the dye injection, which is confirmed by the PIV measurement (not shown here).

Figure 7 shows the time sequence photographs of the meridian section as the process from the formation to shedding of the ring vortex for PAA 0.8 wt% at  $Re_0=1.9$ .  $T$  is the period of the vortex shedding, and  $t=T$  represents the time of just after vortex shedding. Figure 7(a) shows the onset of the ring vortex near the rotating disk. The ring vortex gradually becomes observably larger with time [Figs. 7(b)–7(d)]. From the enlarged view of the ring vortex, it is found that within the ring vortex, the circulating flow is outward near the rotating disk and inward away from the rotating disk. Sometime later, the ring vortex gradually moved away from the rotating disk with time [Figs. 7(e) and 7(f)]. Then the ring vortex was involved in the background secondary flow near the center of the cylinder ( $z/H \approx 0.6$ ) [Fig. 7(g)], and finally disappeared.

With increasing Reynolds number, the ring vortex near the rotating disk becomes nonaxisymmetric. The nonaxisymmetric ring vortex was observed for PAA 0.5, 0.8, and 1.0 wt%, not for PAA 0.1 and 0.2 wt%, in which the elastic number is smaller. The axial height and radial width of the nonaxisymmetric ring vortex are smaller and larger compared to those of the axisymmetric vortex, respectively, which does not depend on the elastic number. In order to clarify the size of the ring vortex quantitatively, however, the velocity measurement would be needed in addition to the flow visualization. Readers will be referred to our study on the PIV measurement in the near future. The sectional visualization of the nonaxisymmetric ring vortex ( $r/R=0-0.6$  and  $z/H=0.7-1.0$ ) for PAA 1.0 wt% at  $Re_0=1.9$  was shown in Fig. 8. In this case, the ring vortex seems to be periodically oscillating in the radial direction, i.e., to sway from side to side.

Figure 9 shows the vortex shedding regime, which was superimposed on the stability boundary diagram of the confined swirling flow presented by Stokes and Boger<sup>20</sup> for Boger fluids. Note that we used  $Re_0$  and  $E_0$  instead of  $Re$  and  $E$  because Stokes and Boger<sup>20</sup> used the constant relaxation time. The dash-dotted line represents the transition to unsteady behavior, and the dotted line represents the boundary between steady Newtonian-like and “reverse” flow regimes. Solid lines represent the upper and lower critical Reynolds numbers for the vortex shedding observed. The region between these solid lines (gray area in Fig. 9) indicates the vortex shedding regime for the PAA solutions used, and it exists in the unsteady flow regime. The vortex shedding cannot be observed below a critical elastic number. The critical values of  $Re_0$ ,  $Re$ , and  $E$  for the vortex shedding observed are presented in Table II. Note that the critical Reynolds number for the vortex shedding was slightly altered by the hysteresis effect and the magnitude of the acceleration of the rotating disk. In the region between the boundary of steady and unsteady flow regimes (dash-dotted line) and the lower limit of the vortex shedding regime (solid line), we confirmed the swirling flow where the secondary flow direction was opposite to that of the Newtonian fluid and in an unsteady state in the vicinity of the central axis, as reported by Stokes and Boger<sup>20</sup> (not shown here).

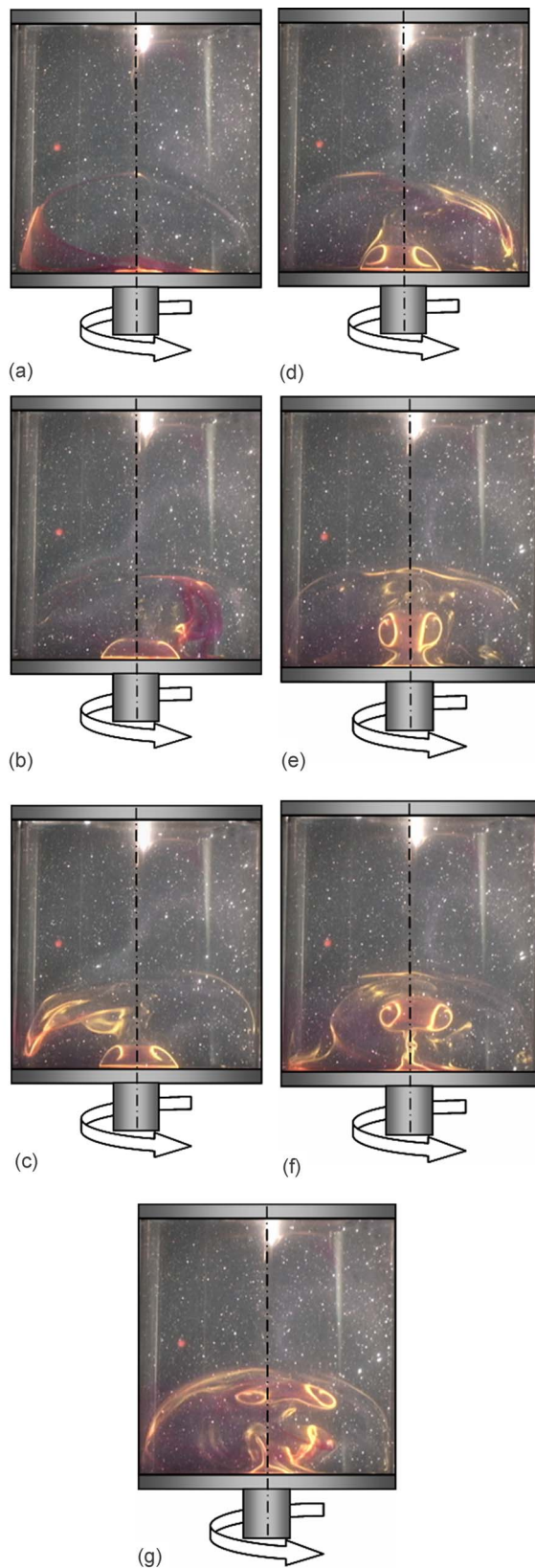


FIG. 7. Process from formation to shedding of ring vortex for PAA 0.8 wt% at  $Re_0=1.9$ : (a)  $t=(T-40)$  s, (b)  $t=(T-20)$  s, (c)  $t=(T-15)$  s, (d)  $t=(T-10)$  s, (e)  $t=T$  s, (f)  $t=(T+1)$  s, and (g)  $t=(T+4)$  s.

Figure 10(a) shows the nondimensional period  $T/(2\pi/\Omega)$  of the vortex shedding. This period increases with the increase of Reynolds number  $Re_0$  for PAA 0.5, 0.8, and 1.0 wt%, while it slightly decreases with  $Re_0$  for PAA 0.1

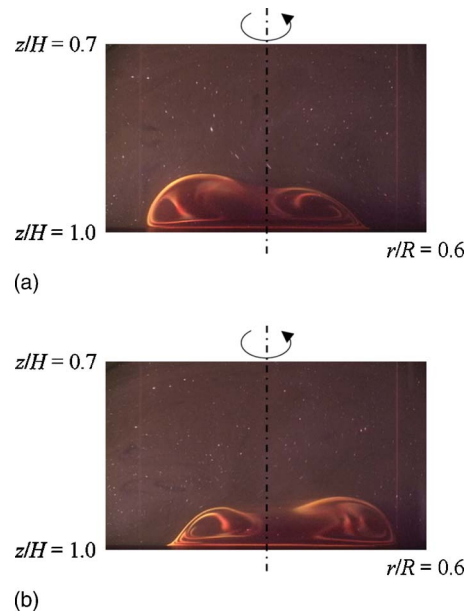


FIG. 8. Sectional flow visualization of nonaxisymmetric ring vortex for PAA 1.0 wt% at  $Re_0=1.9$ : (a) Ring vortex distorted on the left-hand side, (b) ring vortex distorted on the right-hand side.

and 0.2 wt%, in which the elastic number is smaller. On the other hand, Fig. 10(b) shows that the nondimensional period of the vortex shedding  $T/\lambda_m$  increases roughly with the apparent Reynolds number  $Re$ . Note that  $T/\lambda_m$  decreases with increasing  $Re$  for PAA 0.1 and 0.2 wt%, where the nonaxisymmetric ring vortex was not observed. For further discussion of the period of the vortex shedding, however, we would need to introduce the local shear viscosity and relaxation time, which depend on the local shear rate.

**IV. A POSSIBLE VORTEX SHEDDING MECHANISM**

The present study revealed that the vortex shedding could be observed in the confined swirling flow of polymer solutions using the sectional and three-dimensional flow visualization technique. However, the physical mechanism

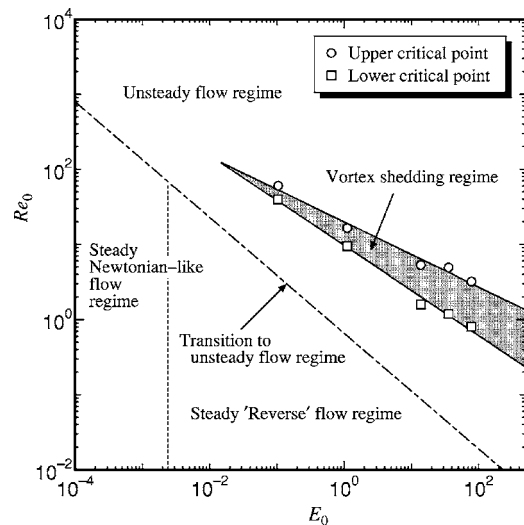


FIG. 9. Vortex shedding regime for PAA solutions.

TABLE II. Critical values of  $Re_0$ ,  $Re$ , and  $E$  for the vortex shedding.

C (wt%)	Upper			Lower		
	$Re_0$	$Re$	$E$	$Re_0$	$Re$	$E$
0.1	61	$2.9 \times 10^2$	$5.0 \times 10^{-3}$	39	$1.6 \times 10^2$	$7.9 \times 10^{-3}$
0.2	17	$2.0 \times 10^2$	$1.5 \times 10^{-2}$	9.4	85	$2.5 \times 10^{-2}$
0.5	5.3	$2.8 \times 10^2$	$2.1 \times 10^{-2}$	1.6	40	$1.6 \times 10^{-1}$
0.8	4.9	$2.5 \times 10^2$	$3.1 \times 10^{-2}$	1.2	23	$2.2 \times 10^{-1}$
1.0	3.2	$2.1 \times 10^2$	$4.1 \times 10^{-2}$	$8.1 \times 10^{-1}$	19	$2.7 \times 10^{-1}$

why the vortex shedding occurs has not been understood well. A possible mechanism for the vortex shedding is as follows. From the flow visualization results (see Figs. 6 and 7), it is deduced that the high shear layer exists at the boundary between the ring vortex and the outer large-scale secondary flow. We confirmed the existence of the high shear layer by using the PIV measurements (not shown here). The high shear layer yields the high shear rate, so that the large first normal stress difference, which is the typical elastic force, would be generated near the outer boundary of the ring vortex. Owing to an elastic effect, an elastic energy may be stored inside the ring vortex near the rotating disk. Eventually, the ring vortex is shed away from the rotating disk to release its energy, when the amount of elastic energy stored inside the ring vortex exceeds a critical value.

The vortex shedding could not be observed below the critical elastic number (see Fig. 9). This may be because the elastic energy is not accumulated enough to induce the vortex shedding. Figure 9 also shows that the lower Rey-

nolds number becomes smaller with increasing elastic number. This indicates that the elastic energy needed for the vortex shedding can be stored at lower Reynolds numbers with increasing the elastic number, i.e., the elastic force. From the result that the period of vortex shedding  $T/\lambda_m$  increases roughly with the apparent Reynolds number  $Re$  [see Fig. 10(b)], it can be deduced that it takes longer to store the elastic energy at larger Reynolds numbers, since the elastic effect becomes relatively smaller compared to the inertia effect. This may result in the longer time of the period of the vortex shedding at larger Reynolds numbers. However, the result that  $T/\lambda_m$  decreases with increasing  $Re$  for PAA 0.1 and 0.2 wt%, in which the elastic effect is relatively weak, cannot be explained by using the concept of elastic energy well.

The study by Min *et al.*<sup>25</sup> supports the mechanism proposed here. These investigators presented the drag reduction mechanism based on the idea of elastic energy storage that is similar to the explanation given above. An extensive velocity measurement on the meridian section and the section parallel to the rotating disk using PIV technique may be necessary to better understand the flow dynamics described in the present study. The study on confined swirling flow in a cylindrical container with a partially rotating disk could be helpful to clarify the mechanism of the vortex shedding. In addition, the other rheological measurements such as the elongational viscosity and the dynamic shear viscosity would be desired.

## V. CONCLUSION

Unsteady swirling flows of polyacrylamide (PAA) solutions in a cylindrical casing with a rotating disk have been investigated by sectional and three-dimensional flow visualizations at relatively high Reynolds numbers. The unsteady flow patterns were classified using the Reynolds and elastic numbers. The main results of the present study may be summarized as follows.

(i) The ring vortex is formed near the center of the rotating disk and grows larger, and it is finally shed in the axial direction. This process is repeated periodically.

(ii) At the higher Reynolds number within the region of the vortex shedding, the ring vortex becomes nonaxisymmetric for PAA 0.5, 0.8, and 1.0 wt%, but not for PAA 0.1 and 0.2 wt%, in which the elastic number is smaller. The nonaxisymmetric ring vortex on the meridian section seems to be periodically oscillating in the radial direction.

(3) The nondimensional period of vortex shedding  $T/(2\pi/\Omega)$  increases with the increase of  $Re_0$  for PAA 0.5, 0.8, and 1.0 wt%, while it decreases with the increase of  $Re_0$  for PAA 0.1 and 0.2 wt%. On the other hand, the period of the vortex shedding  $T/\lambda_m$  increases roughly with the apparent Reynolds number  $Re$ .

## ACKNOWLEDGMENTS

The gear motor with inverter provided by Sumitomo Heavy Industries, Ltd. is gratefully acknowledged. Special thanks are also due to M. Li, A. Sasakawa, and H. Koshino

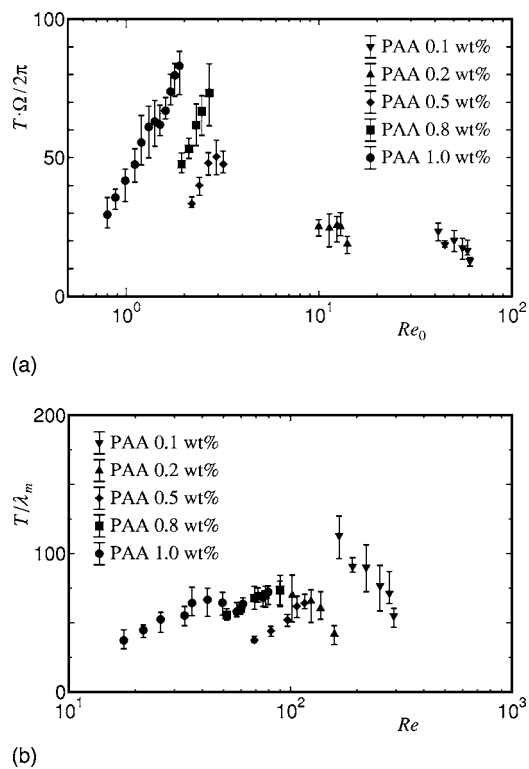


FIG. 10. Nondimensional period of vortex shedding for PAA solutions: (a)  $T/(2\pi/\Omega)$  versus  $Re_0$ , (b)  $T/\lambda_m$  versus  $Re$ .

for their unfailing assistance in the experimental measurements.

- <sup>1</sup>C. T. Hill, "Nearly viscometric flow of viscoelastic fluids in the disc and cylinder system. II: Experimental," *Trans. Soc. Rheol.* **16**, 213 (1972).
- <sup>2</sup>C. Day, J. A. Harris, J. Soria, D. V. Boger, and M. C. Welsh, "Behavior of an elastic fluid in cylindrical swirling flow," *Exp. Therm. Fluid Sci.* **12**, 250 (1996).
- <sup>3</sup>M. P. Escudier and L. M. Cullen, "Flow of a shear-thinning liquid in a cylindrical container with a rotating end wall," *Exp. Therm. Fluid Sci.* **12**, 381 (1996).
- <sup>4</sup>T. Moroi, M. Itoh, K. Fujita, and H. Hamasaki, "Viscoelastic flow due to a rotating disc enclosed in a cylindrical casing (influence of aspect ratio)," *JSME Int. J., Ser. B* **44**, 465 (2001).
- <sup>5</sup>M. Itoh, M. Suzuki, and T. Moroi, "Swirling flow of a viscoelastic fluid in a cylindrical casing," *ASME Trans. J. Fluids Eng.* **128**, 88 (2006).
- <sup>6</sup>J. R. Stokes, L. J. W. Graham, N. J. Lawson, and D. V. Boger, "Swirling flow of viscoelastic fluids. Part 1. Interaction between inertia and elasticity," *J. Fluid Mech.* **429**, 67 (2001).
- <sup>7</sup>J. R. Stokes, L. J. W. Graham, N. J. Lawson, and D. V. Boger, "Swirling flow of viscoelastic fluids. Part 2. Elastic effects," *J. Fluid Mech.* **429**, 117 (2001).
- <sup>8</sup>J. M. Kramer and M. W. Johnson, "Nearly viscometric flow in the disk and cylinder system. I: Theoretical," *Trans. Soc. Rheol.* **16**, 197 (1972).
- <sup>9</sup>J. P. Nirschl and W. E. Stewart, "Computation of viscoelastic flow in a cylindrical tank with a rotating lid," *J. Non-Newtonian Fluid Mech.* **16**, 233 (1984).
- <sup>10</sup>G. Böhme, L. Rubart, and M. Stenger, "Vortex breakdown in shear-thinning liquids: Experiment and numerical simulation," *J. Non-Newtonian Fluid Mech.* **45**, 1 (1992).
- <sup>11</sup>S.-C. Xue, N. Phan-Thien, and R. I. Tanner, "Fully three-dimensional, time-dependent numerical simulations of Newtonian and viscoelastic swirling flows in a confined cylinder. Part I. Method and steady flows," *J. Non-Newtonian Fluid Mech.* **87**, 337 (1999).
- <sup>12</sup>D. A. Siginer, "On the nearly viscometric torsional motion of viscoelastic liquids between shrouded rotating disks," *Trans. ASME, J. Appl. Mech.* **71**, 305 (2004).
- <sup>13</sup>S.-M. F. Chio and H.-C. Chang, "Instability of a Criminale-Ericksen-Filbey fluid in a disc-and-cylinder system," *J. Non-Newtonian Fluid Mech.* **36**, 361 (1990).
- <sup>14</sup>R. G. Larson, "Instabilities in viscoelastic flows," *Rheol. Acta* **31**, 213 (1992).
- <sup>15</sup>A. Öztekin and R. A. Brown, "Instability of a viscoelastic fluid between rotating parallel disks: Analysis for the Oldroyd-B fluid," *J. Fluid Mech.* **255**, 473 (1993).
- <sup>16</sup>J. A. Byars, A. Öztekin, R. A. Brown, and G. H. McKinley, "Spiral instability in the flow of highly elastic fluids between rotating parallel disks," *J. Fluid Mech.* **271**, 173 (1994).
- <sup>17</sup>E. S. G. Shaqfeh, "Purely elastic instabilities in viscometric flows," *Annu. Rev. Fluid Mech.* **28**, 129 (1996).
- <sup>18</sup>A. Groisman and V. Steinberg, "Elastic turbulence in a polymer solution flow," *Nature (London)* **405**, 53 (2000).
- <sup>19</sup>A. Groisman and V. Steinberg, "Elastic turbulence in curvilinear flows of polymer solutions," *New J. Phys.* **6**, 29 (2004).
- <sup>20</sup>J. R. Stokes and D. V. Boger, "Mixing of viscous polymer liquids," *Phys. Fluids* **12**, 1411 (2000).
- <sup>21</sup>Y. Naka, K. Chiba, and K. Nakamura, "Entry flow patterns for polymer solutions through eccentric abrupt contractions," *JSME Int. J., Ser. B* **64**, 2019 (1998) (in Japanese).
- <sup>22</sup>K. Chiba and K. Nakamura, "Instabilities in a circular entry flow of dilute polymer solutions," *J. Non-Newtonian Fluid Mech.* **73**, 67 (1997).
- <sup>23</sup>K. Chiba, R. Ishida, and K. Nakamura, "Mechanism for entry flow instability through a forward-facing step channel," *J. Non-Newtonian Fluid Mech.* **57**, 271 (1995).
- <sup>24</sup>R. B. Bird, R. C. Armstrong, and O. Hassager, *Dynamics of Polymeric Liquids. Volume 1: Fluid Mechanics*, 2nd ed. (Wiley Interscience, New York, 1987), pp. 353–369.
- <sup>25</sup>T. Min, J. Y. Yoo, H. Choi, and D. D. Joseph, "Drag reduction by polymer additives in a turbulent channel flow," *J. Fluid Mech.* **486**, 213 (2003).